Journal of Materials Chemistry A

Kinetic origins of the metastable zone width in the manganese oxide Pourbaix diagram

Journal:	*Journal of Materials Chemistry A*
Manuscript ID	TA-ART-12-2020-012533.R1
Article Type:	Paper
Date Submitted by the Author:	01-Feb-2021
Complete List of Authors:	Chen, Bor-Rong; SLAC National Accelerator Laboratory, SSRL Sun, Wenhao; Lawrence Berkeley National Laboratory, Materials Science Division; University of Michigan, Materials Science and Engineering Kitchaev, Daniil; UC Santa Barbara, Materials Department Stone, Kevin; SLAC National Accelerator Laboratory, SSRL Davis, Ryan; SLAC National Accelerator Laboratory, SSRL Ceder, Gerbrand; University of California Berkeley, Materials Science and Engineering; Lawrence Berkeley National Laboratory, Materials Science Division Schelhas, Laura; SLAC National Accelerator Laboratory, Applied Energy Division; National Renewable Energy Laboratory Toney, Michael; SLAC National Accelerator Laboratory, SSRL ; University of Colorado at Boulder

SCHOLARONE™
Manuscripts

Kinetic origins of the metastable zone width in the manganese oxide Pourbaix diagram

Bor-Rong Chen[1,*], Wenhao Sun[2,3,*], Daniil A. Kitchaev[5], Kevin H. Stone[1], Ryan C. Davis[1], Gerbrand Ceder[2,4], Laura T. Schelhas[6,7], Michael F. Toney[1,8,*]

[1]Stanford Synchrotron Light Source, SLAC National Accelerator Laboratory, Menlo Park, CA 94025, USA
[2]Materials Science Division, Lawrence Berkeley National Laboratory, Berkeley, CA 94720, USA
[3]Department of Materials Science and Engineering, University of Michigan, Ann Arbor, Michigan, 48109, USA
[4] Department of Materials Science and Engineering, UC Berkeley, Berkeley, CA 94720, USA
[5]Materials Department, UC Santa Barbara, Santa Barbara, CA 93117, USA
[6]Applied Energy Division, SLAC National Accelerator Laboratory, Menlo Park, CA 94025, USA
[7]National Renewable Energy Laboratory, Golden, CO 80401, USA
[8]Department of Chemical and Biological Engineering, University of Colorado Boulder, Boulder, CO 80309, USA
[*]Corresponding authors

Abstract

Pourbaix diagrams show solid-aqueous phase stability as a function of *p*H and redox potential and can be a valuable tool to guide the hydrothermal synthesis of transition metal oxides. However, the Pourbaix diagram is based on thermodynamics, and nucleation kinetics are not readily apparent in this framework. Here, we conduct a combined experimental and theoretical study to measure the onset of MnO_2 precipitation from an MnO_4^-(aq) solution at various *p*H conditions, which we then compare against Pourbaix diagram phase boundaries. Using a combination of *in situ* X-ray absorption spectroscopy and X-ray wide-angle scattering, we directly observe the transformation kinetics from tetrahedral MnO_4^-(aq) ion to octahedrally coordinated Mn pre-nuclei, as well as its initiation into crystalline δ'-MnO_2 at various *p*H. The kinetics of octahedral-Mn precursor availability is observed to govern induction times of crystalline MnO_2 nucleation, which results in a Metastable Zone Width in the Mn-H_2O Pourbaix diagram. These results suggest that synthesis conditions often need to be prepared far beyond the phase boundaries in a Pourbaix diagram to initiate crystallization within a reasonable timescale.

■ Introduction

Hydrothermal synthesis is an effective method to produce high-quality crystals with controllable size, shape, phase, and composition[1–3]. Because hydrothermal synthesis proceeds at lower reaction temperatures (< 200 °C) than solid-state synthesis (~1000 °C), it is an appealing and energy-efficient synthesis route for a variety of functional materials, such as metal oxides[4–6], semiconductors[2], zeolites[7], and metal-organic frameworks[8]. Similar to how temperature-composition phase diagrams are used to help guide solid-state synthesis, Pourbaix (*E*-*p*H) diagrams could, in principle, be used to guide hydrothermal synthesis. The Pourbaix diagram shows solid-aqueous phase stability as a function of *p*H and redox potential, *E*, which could help to inform a solid-state chemist which aqueous conditions would be most likely to yield the successful hydrothermal synthesis of a desired phase.

However, because hydrothermal synthesis is a low-temperature synthesis route, reactions often exhibit slow transformation kinetics, which can result in the formation of long-lived metastable phases[9,10]. When hydrothermal synthesis yields products that differ from the predictions of a Pourbaix diagram, it can be difficult to ascertain the thermodynamic or kinetic origins of this disagreement. In other words, it is challenging to confirm if the Pourbaix diagrams are inaccurate, and in need of revised thermochemical data[11–14], or if there are slow reaction kinetics that result in the nucleation and persistence of non-equilibrium reaction products[10]. Further confounding the issue is the fact that hydrothermal synthesis is typically performed in a closed 'black-box' reactor[15,16] with the consequence that the reaction mechanisms[17–19] and kinetics[20–22] are difficult to track. As a result, the cause-and-effect of synthesis parameters is often interpreted *ex situ*, in which the evolution from the starting precursors to ending products are not observed.

In this work, we conduct careful *in situ* measurements on the kinetics of phase transformation and use the results to infer the phase boundaries on a Pourbaix diagram. Specifically, we investigate the transformation kinetics of an MnO_4^-(aq) precursor to MnO_2(s) at a variety of *E* and *p*H conditions within the MnO_2 stability region, which we compare against the MnO_4^-(aq)/MnO_2(s) phase boundary on a Pourbaix diagram. To observe the nucleation processes in real-time, we utilize a combination of *in situ* synchrotron X-ray scattering (WAXS) with X-ray absorption spectroscopy (XAS) to monitor the transformation reaction[23,24]. The WAXS captures the onset of the crystalline MnO_2 phases (crystalline size >~ 5nm), and XAS reveals the hydrolysis and change in molecular conformation of the precursors [25–28], which is invisible to WAXS.

Our results reveal that within the MnO_2 stability region on the Pourbaix diagram, there exist two qualitatively distinct regions of precipitation kinetics. For *p*H < 2, we find that the induction time to MnO_2 precipitation is in the range of 5 to 35 min, with decreasing induction times with more acidic solution. Surprisingly, we observe a sharp boundary at *p*H > 2, where even though MnO_4^-(aq) remains supersaturated with respect to MnO_2, the solution can persist for over 9 hr without WAXS-observable MnO_2 crystallization. The observation that the thermodynamically-preferred phase does not form is consistent with the concept of the Metastable Zone Width (MZW)[29,30], where a precursor has too low of a steady-state nucleation rate, J_{st}, to initiate precipitation. There is a kinetic and a thermodynamic term in J_{st}, with the kinetic term proportional to the rate of precursor availability, and the thermodynamic term depending on the competition between the surface energy and bulk driving force in the nucleation barrier. Here we argue that the MZW in the manganese oxide system originates from kinetic limitations, rather than thermodynamic limitations. Specifically, we argue that the transformation of tetrahedrally-coordinated Mn in MnO_4^-(aq) to octahedrally-coordinated Mn in MnO_2 is a kinetically rate-limiting process, which governs the nearly discontinuous induction time of MnO_2 as a function of *p*H.

Although MZWs have been routinely investigated in the precipitation of inorganic sparingly-soluble salts and organic molecular crystals [29–31], there has not been a rigorous investigation of the MZW in redox-active

transition metal oxides. Our observation and interpretation of the MZW in a Pourbaix diagram provides fundamental insights into the induction times, driving forces, and non-equilibrium crystallization pathways of redox-active metal oxides in water. Recently, there have been many efforts to achieve more accurate Pourbaix diagrams, both from first-principles DFT and from experimental calorimetry[11–14]. Oftentimes, these studies are motivated by statements that the experimental synthesis results deviate from the expectation set by the thermodynamic Pourbaix diagram. Our results here suggest that important kinetic considerations should be taken into account when evaluating inconsistencies between the thermodynamic Pourbaix diagram and an actual crystallization experiment.

■ Induction Times and the Metastable Zone Width

The Pourbaix diagram is a thermodynamic phase diagram, which shows solid-aqueous equilibria as a function of *p*H and redox potential, *E*. When a precursor (such as MnO_4^-(aq)) is placed under *E* and *p*H conditions where another phase is stable (such as MnO_2(s)), there will be a thermodynamic driving force to drive the transformation from the metastable precursor to the equilibrium product[32,33]. However, even when the precursor is metastable with respect to transformation to a product phase, slow reaction kinetics may result in the precursor persisting in a metastable state. On a phase diagram, the region where a transformation is thermodynamically preferred but kinetically obstructed is referred to as the "Metastable Zone Width (MZW)."

In classical nucleation theory, there are two possible origins for the MZW[34,35], as summarized in Figure 1(a). The steady-state nucleation rate in a redox-active system can be expressed as $J_{st} = A\ exp\ (-\Delta\Psi_c / k_BT)$. In this expression, we use the Pourbaix free energy (Ψ) instead of the Gibbs free energy (G) that is conventionally used. Here, Ψ is the appropriate thermodynamic potential for the Pourbaix diagram[32,33]. The term *A* represents a kinetic pre-factor, whose physical origins are governed by solute availability to form the nucleus and the monomer attachment frequency[36]. The $\Delta\Psi_c$, is referred to as the "thermodynamic" nucleation barrier, which is expressed as $\Delta\Psi_c \sim \gamma^3/(\Delta\Psi_{bulk})^2$. The physical meaning of equation is the ratio between two thermodynamic quantities: the surface energy (γ), and the thermodynamic driving force ($\Delta\Psi_{Bulk}$). The units of J_{st} is nuclei·time^{-1}·volume^{-1}, and its inverse, $\tau = 1 / (J_{st} \cdot V)$, is the characteristic induction time before the first nucleation event for a given reactor volume (V). The MZW can therefore originate kinetically from the lack of precursor solute, or thermodynamically, due to the height of the nucleation barrier.

To evaluate the induction time and MZW on a Pourbaix diagram, here we measure the transformation of the MnO_4^-(aq) precursor into an δ'-MnO_2(s) product ($K_{0.33}MnO_2 \cdot 0.66H_2O$), at varying *p*H and redox potential *E* (see Figure 1(b) for the atomic structures). The δ'-MnO_2 is a subset of a large family of layered δ-MnO_2 (birnessite-like) phases, where the layer spacing is determined by hydration and ion intercalation in between the layers[33]. In order to measure the induction times and MZW of this phase transformation, we performed *in situ* WAXS and XAS to monitor the transformation process from MnO_4^- to δ'-MnO_2 at *p*H values ranging from 0.5 to 2.6.

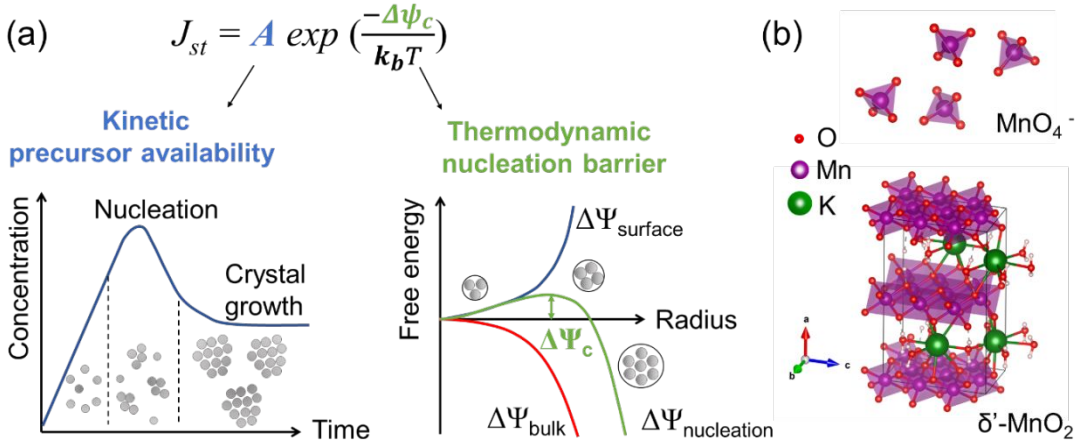

Figure 1. Schematics showing the factors controlling the steady-state nucleation rate and atomic structures of the Mn-species discussed in this work. (a) The two major factors, precursor availability and nucleation barrier, controlling the kinetic and thermodynamic aspects of steady-state nucleation rate (J_{st}), respectively[34,35]. (left) The precursor availability can be interpreted as the abundance of solute supply for nucleation to happen. The LaMer nucleation model describes the correlation between precursor concentration (represented by the gray balls) as a function of time. (right) The nucleation barrier ($\Delta\Psi_c$), defines the minimum radius that allows a nuclei to be stable. $\Delta\Psi_c$ originates from the competition between bulk free energy ($\Delta\Psi_{volume}$) and surface energy ($\Delta\Psi_{surface}$) of the nuclei. (b) Atomic structures of permanganate ion (MnO_4^-) and δ'-MnO_2 ($K_{0.33}MnO_2 \cdot 0.66H_2O$) discussed in this paper. More discussion about the δ'-MnO_2 phase can be found in our previous work[33].

■ Experimental

Sample Preparation. The experimental conditions in this report were adapted from our previous publication[33]. In this experiment, 1 mmol $KMnO_4$ (Sigma-Aldrich, 99.0%) was dissolved in 5 mL of HNO_3 solution. The concentration of Mn in the solution was 0.2 M. The *p*H value in the solution was adjusted by varying the concentration of HNO_3. The *p*H and oxidation reduction potential (ORP) values were measured immediately after the solution was completely mixed (see Supporting Information 1). The prepared $KMnO_4$ solution was loaded into a glass capillary tube, which is used as the hydrothermal reaction vessel. In the WAXS experiments, the capillary tube has 0.1 mm wall thickness, 1 mm diameter, and 75mm length (Kimble 2502). The filling volume in the capillary was approximately 75 %. Then, both ends of the glass capillary were flame-sealed. For the XAS experiment, the procedures were the same as described above, except that capillary vessels with a thinner wall thickness were used (Charles Supper, 0.01 mm wall thickness, 0.7 mm diameter, and 80 mm length) to increase the X-ray transmission at the Mn K edge.

***In situ* X-ray Measurements.** The *in situ* WAXS and XAS experiments were carried out at beamline 11-3 and 4-1, respectively, at the Stanford Synchrotron Radiation Lightsource (SSRL). During the hydrothermal reaction, the solution was heated to 120 °C or 160 °C until crystallization was observed. The heating profiles are consistent for all samples heated at 120 °C and 160 °C, respectively. To hold the hydrothermal capillary reactor at the beamline, we have designed a sample holder/heater (see Supporting Information 2 for further details). In the WAXS experiments, the incident wavelength used was 0.9744 Å (12.7 keV). During the reaction, time-resolved 2D scattering patterns were collected consecutively using a Rayonix 225 detector, with each image exposed for 1 min. Data reduction and integration were completed using the GSAS-II

software package[37]. To gain a better signal to noise ratio while determining the onset of MnO_2 crystallization, every three scattering profiles were averaged. However, for the *p*H 0.5 and *p*H 1.1 data sets at 160 °C, the crystallization occurs quickly at the first few minutes. Therefore, the scattering profiles for these two conditions were not averaged to gain better time resolution.

The XAS experiments were carried out at Mn K edge (6539 eV). The capillary reactor and heating profile were the same as those used in the WAXS experiments. The XAS reaction was carried out at 120 °C. The XAS data were collected in fluorescence mode using a Lytle-type fluorescence-yield ion chamber detector. Data processing and linear combination fitting were completed using the ATHENA and ARTEMIS software packages[38]. For further information about the setup, please see Supporting Information 2. Two Mn reference samples, dry δ'-MnO_2 powder and 0.2M $KMnO_4$ aqueous solution, were used in the XAS measurements. To make the dry δ'-MnO_2 powder, 3 mmol $KMnO_4$ was dissolved in 15 mL 0.2 M HNO_3 (aq), then reacted in a Parr autoclave (model 4749) for 24 hr. This procedure follows the $[K^+] = 0.33M$ reaction pathway reported in our previous publication[33].

■ Results

MnO_2 Crystallization Onset Analyzed by WAXS. From the WAXS measurements, we define the onset time of the δ'-MnO_2 phase by the appearance of the (200) diffraction peak at q = 0.85 $Å^{-1}$. Figure 2 selectively summarizes the evolution of δ'-MnO_2 (200) peaks and the integrated intensity as a function of reaction time and *p*H in the solution. The δ'-MnO_2 (200) peaks were fitted by a Lorentzian function, and the onset of δ'-MnO_2 is defined as the time point that the peak shape can be meaningfully fitted. The onset times at different solution conditions for all of the reaction conditions are listed in Table S2 of Supporting Information 3. An example of full diffraction profiles evolving over time can be found in Figure S3 in Supporting Information 4.

When *p*H < 2, the integrated intensity of the (200) peak appreciably increases with reaction time after the δ'-MnO_2 nucleation onset. For the 160 °C reactions, the δ'-MnO_2 (200) onset at *p*H 0.5 and 1.1 are both around 5–6 min. Due to the time resolution of the X-ray data acquisition (1 min/frame), these two onset points are indistinguishable. As the *p*H increases to 1.3, the onset time is delayed to about 20 min, and then further delayed to 29 min at *p*H 1.8. For the 120 °C reactions, the crystallization onset is generally slower than that of 160 °C due to the slower kinetics. The increasing trend of the onset time is also less pronounced. Across *p*H 0.5 to *p*H 1.7, the onset time slowly increases from 26 min to 35 min.

In contrast, the behavior of the samples when *p*H ≥ 2 is significantly different from that of *p*H < 2. At *p*H 2.6, the (200) peak is not observable by *in situ* WAXS even after ~9 hr (539 min) and ~15 hr (908 min) of reaction at 120 and 160 °C, respectively. In a parallel *ex situ* hydrothermal reaction at *p*H 2.6 and 120 °C, no visually observable precipitation is found even after 5400 min (3.75 days). At *p*H 2, although there is a very weak peak observed around q = 0.85 $Å^{-1}$ after 83 min (120 °C) and 300 min (160 °C) of the reaction, the intensity of this peak does not show any trend of significant or consistent growth up to ~9.6 hr (576 min) (see Table S2 and Figure S2 in Supporting Information 3). Thus, we conclude that the *p*H ≥ 2 samples do not have a WAXS-observable onset point. This remarkable difference between the onset for lower and higher than *p*H 2 will be discussed below.

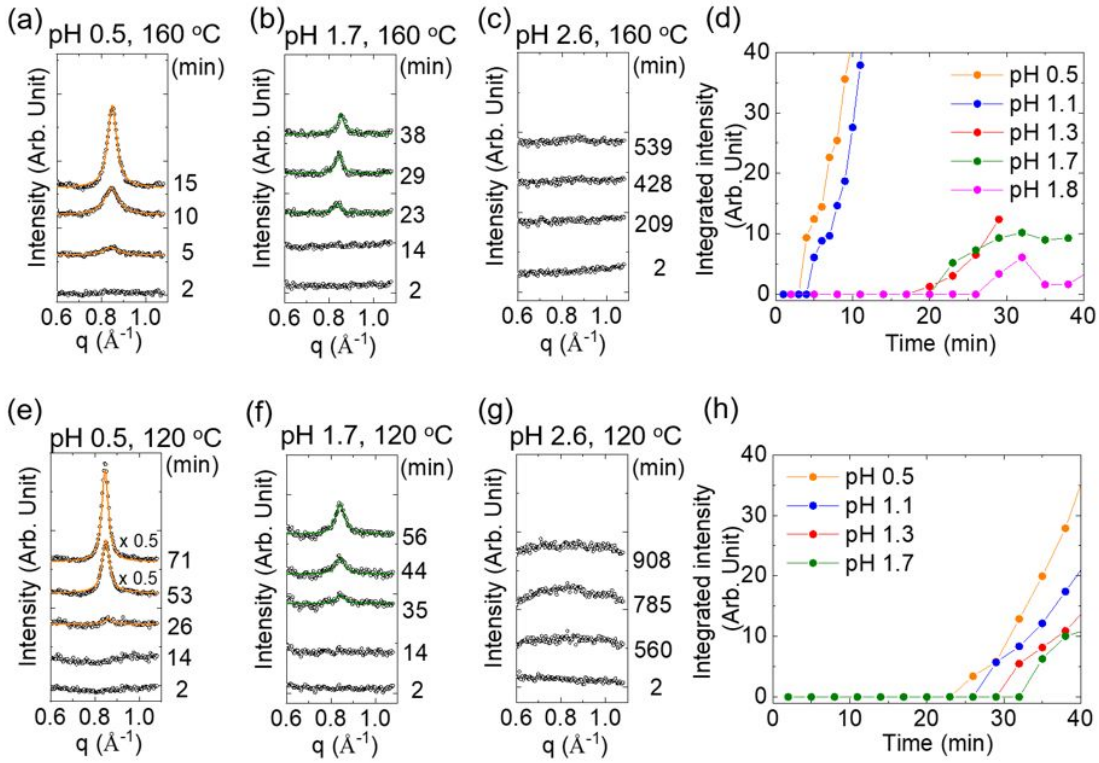

Figure 2. Evolution of the δ'-MnO_2 (200) peak and onset of crystallization. The δ'-MnO_2 (200) peak evolution at representative *p*H and time points at 160 °C (a-c) and 120 °C (e-g), showing the onset point and intensity growth after. The experimental data and the fits are shown by the open circles and solid lines, respectively. The onset of δ'-MnO_2 is defined as the time point that the (200) peak shape can be meaningfully fitted by a Lorentzian function. The integrated intensity of the (200) scattering peak in the first 40 min of the hydrothermal reaction at 160 °C(d) and 120 °C(h). For the data after 40 min and not presented here in the manuscript, please see Figure S2 in Supporting Information 3.

Reaction Sequence from MnO_4^- to MnO_2 Analyzed by XAS. To further investigate the reaction *before* the crystallization of δ'-MnO_2 in the solution, the X-ray absorption near edge structure (XANES) region of the XAS was measured. The XANES region is sensitive to the chemical state of Mn reducing from Mn^{7+} (MnO_4^-) to Mn^{4+} (MnO_2). Together with reference spectra and the features in the extended X-ray absorption fine structure (EXAFS) region, the chemical state of Mn can be further correlated to the local coordination of Mn. This correlation allows a detailed study of the transition from tetrahedrally-coordinated MnO_4^- (Mn_{tet}) to octahedrally-coordinated MnO_2 (Mn_{oct}) independent of the formation of extended nuclei, especially for conditions that have similar onset times (e.g., *p*H 0.5 and 1.1 at 120 °C) or lack of a WAXS-onset within the time scale of our observation (e.g., *p*H 2.6 at 120 °C).

Following the discussion above, we focus on using Mn XANES to analyze the transition trend of *p*H 0.5, 1.1, and 2.6 samples at 120 °C. As shown in Figure 3(a-c), the oxidation state of Mn changes during the crystallization, as revealed by the shape change of the spectra. The reference spectra of 0.2 M $KMnO_4$ (aq) and dry δ'-MnO_2 powder are shown in Figure 3(d), representing Mn in tetrahedral (Mn_{tet}) and octahedral coordination (Mn_{oct}), respectively. At room temperature (RT), the initial spectra (t=0) for all three *p*H values are characterized by a single, strong pre-edge peak around 6542 eV, which is the primary feature of

Mn^{7+} in tetrahedrally coordinated MnO_4^- ions[39–42]. As the solution is heated and after the hydrothermal reaction starts, this pre-edge peak gradually loses intensity, indicating a gradual increase in the averaged Mn coordination number[41]. In the cases of *p*H 0.5 and *p*H 1.1, the single peak pre-edge eventually transforms into a doublet, representing the octahedrally coordinated MnO_6 in the δ'-MnO_2 structure[40,43]. The shapes of the endpoint spectrum for *p*H 0.5 (70 min) and *p*H 1.1 (85 min) are very similar to that of the dry δ'-MnO_2 reference spectrum in Figure 3(d), with subtle differences attributed the solvation environment in the solution[44,45]. To further confirm that the XAS features observed in the endpoint spectrum for *p*H 0.5 and *p*H 1.1 are the δ'-MnO_2 structure, we analyzed the extended X-ray absorption fine structure (EXAFS) region of the XAS spectrum and compared the results with the dry δ'-MnO_2 reference (Supporting Information 5). The EXAFS data show that the structural features of the δ'-MnO_2 phase were developed at both endpoint spectra. Two peaks representing the Mn–O (~1.9 Å) and Mn–Mn (~ 2.8 Å) nearest-neighbor bonds in the δ'-MnO_2 phase are clearly seen, confirming the formation of the δ'-MnO_2. To further investigate the Mn coordination environment change during the reaction, the *in situ* EXAFS data of the *p*H 1.1 sample are presented in Supporting Information 6. The EXAFS data, after comparison to the references, show a continuous and gradual transition from Mn_{tet} in MnO_4^-(aq) to Mn_{oct} in δ'-MnO_2(s). This observation is also consistent with the XANES and WAXS results.

In the case of *p*H 2.6, although the single pre-edge peak decreases over time, it does not transform into the double peak as in the low *p*H cases over the course of 900 min reaction time. This result is consistent with the WAXS data showing that no visible diffraction peak for δ'-MnO_2 was observed up to 908 min.

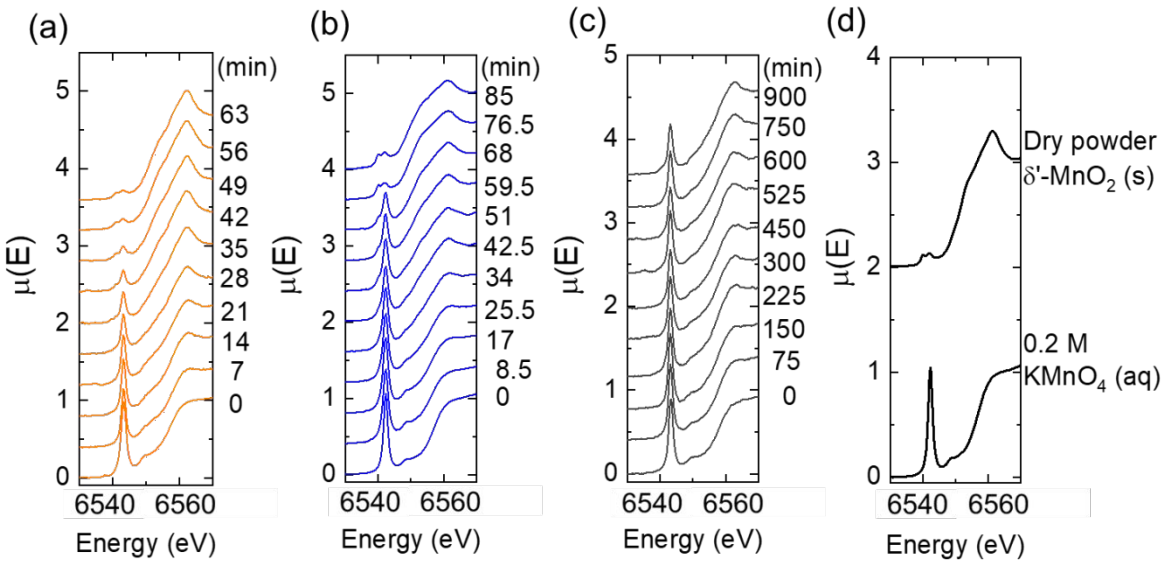

Figure 3. Mn K edge spectra evolution at varying *p*H. (a-c) The Mn K edge of (a) *p*H 0.5 (b) *p*H 1.1, and (c) *p*H 2.6 at 120 °C as a function of reaction time. The data labeled 0 min represent the spectra acquired at room temperature before starting the hydrothermal reaction. (d) Reference spectra of 0.2 M $KMnO_4$ water solution (Mn_{tet}) and dry δ'-MnO_2 powder (Mn_{oct}).

Given that Mn species in different oxidation states result in Mn K edge shapes that are distinctive from MnO_4^- and MnO_2[46], and that the transition in Figure 3 is gradual and smooth from Mn^{7+} (MnO_4^-) to Mn^{4+} (MnO_2), we conclude that the concentrations of other Mn species (e.g. Mn^{2+}, Mn^{3+}….), if any, are dilute. Therefore, the atomic fraction (F) of Mn_{tet} and Mn_{oct} during the transition process can be obtained from linear combination analysis by assuming a) $F_{Mn_{tet}} + F_{Mn_{oct}} = 1$ and b) the Mn^{7+} measured are Mn_{tet} and Mn^{4+} are Mn_{oct}. The two end member components used in the fitting are the initial room temperature spectra of the reaction solutions at a given *p*H and the dry δ'-MnO_2 powder. In order to take the solvation environment into account, the endpoint spectra of pH 0.5 (70 min) and *p*H 1.1 (85 min) were also used in the fitting and compared against to the results using the dry δ'-MnO_2. Representative data points for the two fitting results are compared in Figure 4 and show a good agreement with the data and each other. A complete fitting dataset can be found in Supporting Information 7.

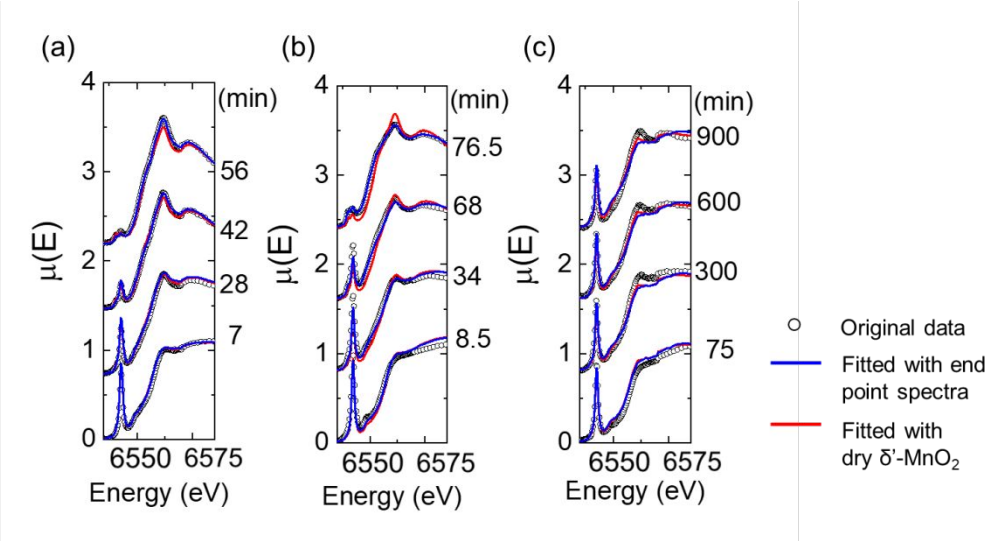

Figure 4. Linear combination fitting results of the Mn K edge spectra. Representative fitting results for (a) *p*H 0.5, (b) *p*H 1.1, and (c) *p*H 2.6, showing the experimental data (open circles), fit with the refence dry δ'-MnO_2 power (red line), and fit with endpoint scans of each of the reactions (blue line). For *p*H 2.6, due to the fact that the edge did not reach the δ'-MnO_2 endpoint, the 85 min spectrum in *p*H 1.1 was used as an endpoint instead.

The results of the linear combination analysis are presented in Figure 5. The fraction of Mn_{tet} decreases linearly over time, and the consumption rate decreases with higher *p*H, especially for *p*H 2.6. For *p*H 0.5 and pH 1.1, although the WAXS results do not have the resolution to distinguish the onset time, the linear combination fitting shows that Mn_{tet} decreases faster for *p*H 0.5. The XAS data do not provide information on δ'-MnO_2 onset directly. In order to compare the transition trend obtained using XAS together with the trend obtained using WAXS, we define the half-life of the atomic fraction of Mn_{tet} as a proxy for the onset time. The half-life of Mn_{tet} for solutions with different *p*H is summarized in Table S3 in Supporting Information 8.

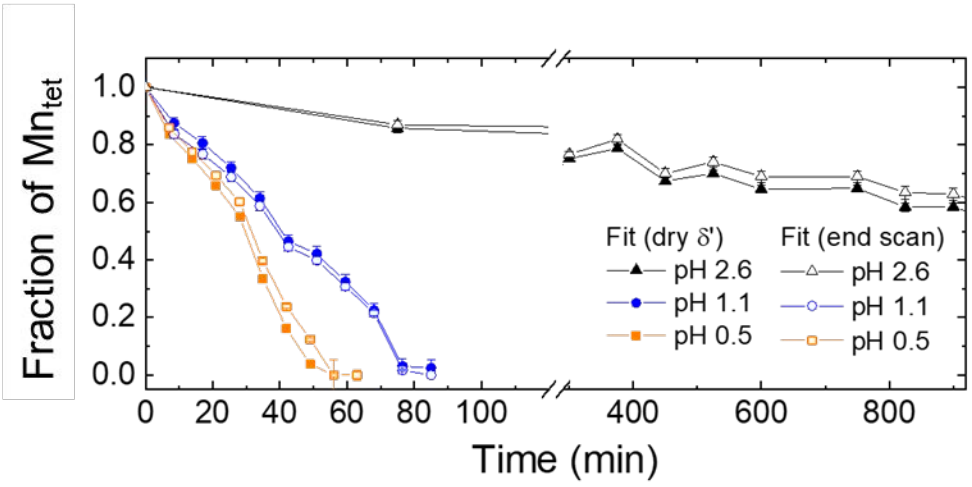

Figure 5. **Atomic fraction Mn_{tet} along with reaction time.** Atomic fraction as a function of reaction time is obtained from linear combination fitting of the Mn K edge spectra. Filled and open symbols represent results obtained by using dry δ'-MnO_2 power and endpoint scans, respectively.

■ Discussion

Metastable Zone Width in the redox active Mn-O-H system. So far, we have measured the trend of δ'-MnO_2 crystallization using WAXS and XANES at different *p*H values. The δ'-MnO_2 onset time from WAXS and XAS as a function of solution *p*H is summarized altogether in Figure 6(a). Here, an important discovery is that in the *p*H ≥ 2 region, there is no *in situ* WAXS observable δ'-MnO_2 onset for at least 9 hrs of reaction time. As the *p*H decreases below *p*H 2, nucleation can initiate within ~35 minutes. The *p*H values investigated here are all much lower than the equilibrium phase boundary between MnO_4^- and MnO_2 on the Pourbaix diagram[32,33], which occurs near *p*H ~ 5 –7 and E ~ +1.3 – +1.1V (see Figure S7 in Supporting Information 9) for the Mn concentration in our experiment (0.2 M). To better illustrate the concept of the MZW, we mark down the reaction conditions in this study onto a conventional Pourbaix diagram, as shown in Figure 6(b). The green dots show the experimental conditions where crystallization is observed, and the red dots represent conditions where nucleation is not observed even after 9 hours. The boundary of the MZW is located in between the green and red dots, marked by the white dashed line. For further visualization, we add a Ψ axis in Figure 6(c) to show the projection of the conventional Pourbaix diagram as well as the reaction conditions from the Pourbaix free-energy space[32,33] (see Supporting Information 11 for related description of Ψ). Notice that the "electrochemical saturation" caused by *p*H reduction needs to be significantly far beyond the equilibrium boundary between the MnO_4^- and δ'-MnO_2 to result in crystallization, as shown by the green arrow in Figure 6(b). The fact that the MnO_4^- precursor can persist in a metastable aqueous state, even in a region of the Pourbaix diagram where MnO_2 is stable, is a demonstration of the Metastable Zone Width (MZW)[29,30]. The boundary of the MZW is observed in our experiment around *p*H 2, as shown in the white dashed line in Figure 6(b) and (c).

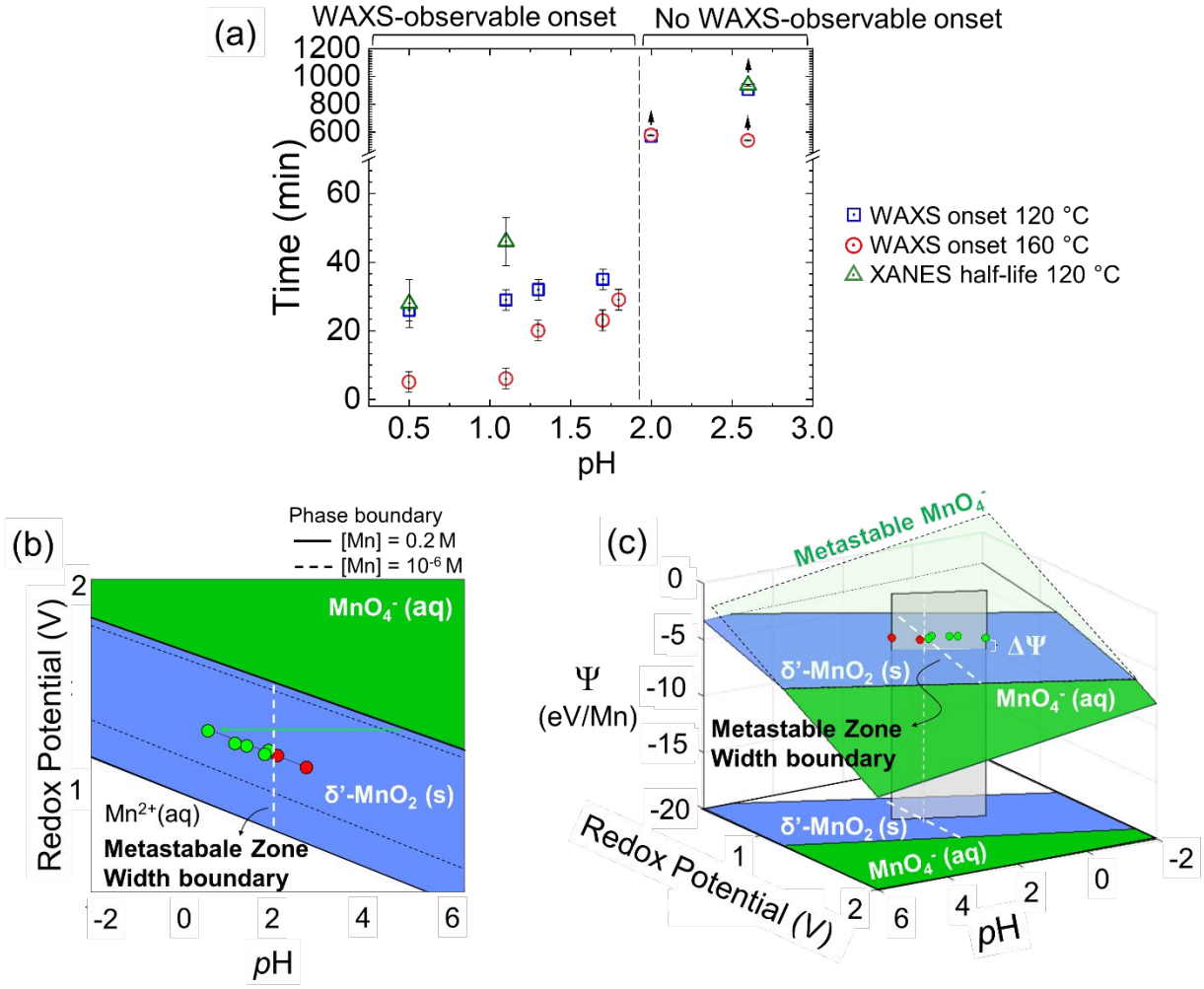

Figure 6. **Trend of MnO_2 onset time and the metastable zone width.** (a) A summary of the δ'-MnO_2 onset time and Mn_{tet} half-life as a function of *p*H and reaction temperature, measured using WAXS and XANES, respectively. The datapoints with upward arrows represent the absence of δ'-MnO_2 onset when the *in situ* WAXS observation ended. (b) The boundary of metastable zone width (white dashed line) marked on a section of the Mn Pourbaix diagram including the MnO_4^-(aq) and δ'-MnO_2 phases (see Figure S7 in Supporting Information 9 for the full diagram). The Pourbaix diagram is shown at the experimental Mn concentration of 0.2 M. A comparison of the phase boundary at [Mn] = 10^{-6} M is shown in black dashed lines. The green dots show the experimental conditions where crystallization is observed, and the red dots represent conditions where nucleation is not observed even after 9 hours. (c) Diagram showing the Pourbaix free-energy landscape above Figure 6(b), illustrating the electrochemical supersaturation (ΔΨ) of MnO_4^-(aq) relative to δ'-MnO_2. The thermodynamic driving force (ΔΨ) does not change significantly in the vicinity of *p*H 2, implying that the thermodynamic effect is not the main cause of the induction time difference.

From a kinetics perspective, our *in situ* XANES observations in Figure 5 directly demonstrate that the kinetics of steric conversion from tetrahedral MnO_4^- to the octahedral MnO_2 environment is dependent on the *p*H. Figure 5 shows that lower *p*H leads to a faster conversion rate, qualitatively consistent with a Le Chatelier-type effect in the reaction:

$$4MnO_4^-(aq) + 4H^+ \rightarrow 4MnO_2(s) + 2H_2O + 3O_2\,(g)\ldots\text{Eq. (1)}$$

This effect suggests that the mechanistic origin of the MZW may be the slow kinetic availability of tetrahedral-Mn precursor transforming into octahedral-Mn. Moreover, by comparing the XANES and the WAXS measurements, the Mn_{tet} to Mn_{oct} conversion begins immediately at the beginning of the experiment even before a signal appears for the crystalline δ'-MnO_2 phase. At 120 °C, the onset of MnO_2 crystallinity in the WAXS measurements is when the fraction of tetrahedral MnO_4^-(aq) has decreased to approximately 54% (pH 0.5) and 66% (pH 1.1) of its starting concentration (see Supporting Information 10 for the interpolation). This Mn_{tet} range, from 50 to 70 %, is likely to be a critical conversion threshold for MnO_2 crystallization to begin. The fact that higher temperatures (160°C vs 120°C) reduced the induction time also points to the role of kinetics in driving this Mn-coordination conversion.

Based on the XANES results, we propose a plausible mechanism in Figure 7(a) to hypothetically describe the nucleation process of MnO_2, even though the detailed atomic structure change of this conversion could not be definitively resolved with the current data due to the coarse time and energy resolution. Following an initial agglomeration of MnO_4^- ions, some of the Mn_{tet} may convert to Mn_{oct}, either by linking neighboring oxygen atoms with another MnO_4^- or by hydrolysis. As the Mn_{tet}-Mn_{oct} assembly is reduced, this process leads to the formation of edge-sharing MnO_6 octahedra. These steps eventually result in the condensation of a δ'-MnO_2 crystal observable through WAXS. To construct a more robust model for the cluster formation process, as well as to quantitatively measure the relative concentrations between the precursors and products, *in situ* techniques with higher time and structural resolution will be valuable, such as quick-EXAFS or pair distribution function (PDF)[28,47]. These techniques could also be used to investigate the potential influence of anion on the reaction kinetics. Previous *ex situ* works on MnO_2 hydrothermal synthesis suggest that replacing HNO_3 with HCl or H_2SO_4 does not change the end product of the reaction pathway[48], but the Cl^-(aq) or SO_4^{2-}(aq) counterions in the solution might change the oxidation-reduction potential of the solution, and therefore change the reaction kinetics.

During the three-step MnO_2 nucleation process shown in Figure 7(a), the solute availability of Mn_{oct} needed to initiate MnO_2 crystallization is limited by the transformation rate of Mn_{tet} into Mn_{oct}. This concept of a precursor-limited intermediate is reminiscent of concepts from "non-classical nucleation theory", where a "dense liquid" pre-nucleation precursor precedes the formation of the crystalline product[49–52]. The mechanism in the MnO_2 system here is different than other non-classical nucleation mechanisms explored in the field, which have focused on ionic aggregation or liquid-liquid separation of sparingly-soluble salts[50,53]. In these simple salts, the ions do not change oxidation states between their solvated aqueous state and their crystalline coordination environment. However, in the MnO_2 system, the availability of Mn_{oct} requires the electrochemical reduction and coordination change of the tetrahedral MnO_4^-(aq) ion. This redox-mediated kinetic limitation in Mn_{oct} solute availability is a new mechanism for the origins of an MZW, and is special to redox-active metal oxide systems.

To further support our argument that the MZW originates from kinetic limitations, rather than thermodynamic limitations, we compute the thermodynamic driving force (ΔΨ) between MnO_4^-(aq) to δ'-MnO_2 at the measured *E* and *p*H conditions in the very beginning of the reaction (See Supporting Information 11 for more details about ΔΨ and related calculations). We visualize this ΔΨ in Figure 6(c), where the Pourbaix free energy of MnO_4^-(aq) relative to that of δ'-MnO_2 is shown for the various *E* and *p*H

conditions investigated experimentally. The water-oxidation line is nearly parallel with the MnO_4^-/MnO_2 phase boundary. At the various *p*H/E conditions we tested, the $\Delta\Psi$ does not change significantly between *p*H > 2 and *p*H < 2. In short, the magnitude of $\Delta\Psi$ does not explain our observation that *p*H influences the MnO_4^- consumption rate and crystallization onset. Nonetheless, this would not detract from the kinetic arguments above, which provide a suitable rationalization of the observed MZW phenomenon.

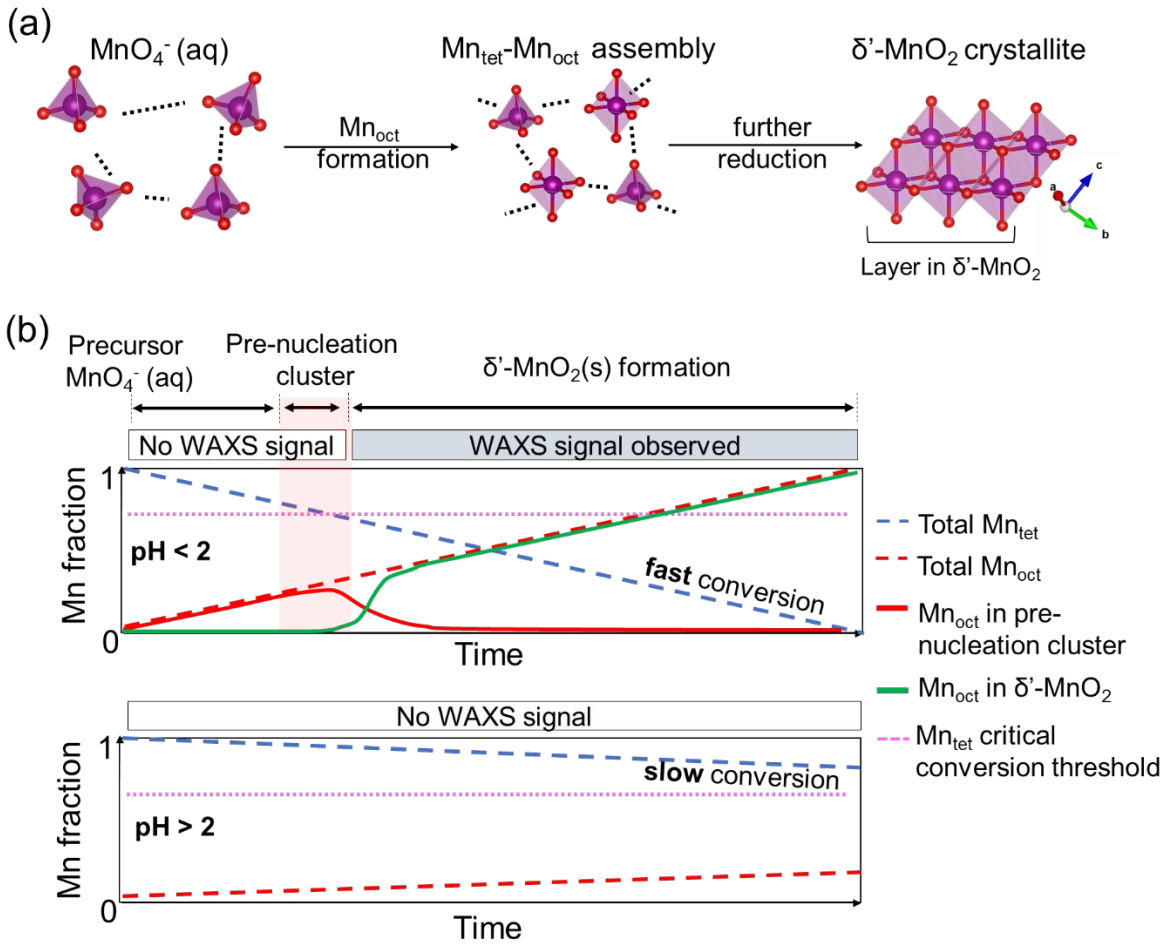

Figure 7. Hypothetical mechanism of δ'-MnO_2 formation at the early stages. (a) Individual MnO_4^- ions in the solution agglomerate, forming a pre-nucleation assembly consisting of Mn_{tet} and Mn_{oct}. Upon further reduction, edge-sharing MnO_6 octahedra form, eventually transforming to solid δ'-MnO_2. (b) A schematic of the development of δ'-MnO_2 along with the atomic fraction of MnO_4^- (Mn_{tet}) and MnO_6 (Mn_{oct}) during the hydrothermal synthesis. The linearly decreased $Mn_{tet/oct}$ fraction in the solution is corresponding to the XANES data shown in Figure 5. As the concentration of the Mn_{tet}-Mn_{oct} pre-nucleation assembly passes the critical conversion threshold, the nucleation of MnO_2 solid begins. In the case of pH > 2, the conversion of Mn_{tet} to Mn_{oct} is too slow, therefore the critical conversion threshold cannot be reached within an observable time frame. This schematic demonstration is adapted from previous works of Smeets *et al*.[50] and Gebauer *et al*.[51].

Reaction order of MnO_4^- reduction. An understanding of the reaction order of Mn_{tet} to Mn_{oct} conversion can serve as a quantitative foundation to anticipate induction times in the MZW of the manganese Pourbaix diagram. During the hydrothermal reaction, the fraction of Mn_{tet} decreases linearly, as shown in Figure 5. To determine whether this linear decrease may be interpreted as a signature of zero-order reaction kinetics, we briefly review the decomposition mechanisms of MnO_4^- reported in the literature and compare these results to ours.

In acidic conditions, the thermal decomposition of MnO_4^-(aq) into MnO_2(s) is conventionally understood to proceed via the Guyard reaction[54–57]:

$$2MnO_4^- + 3Mn^{2+} + 2H_2O \rightarrow 5MnO_2(s) + 4H^+ \ldots \text{Eq. (2)}$$

where Mn^{2+} ions are produced by the equilibrium:

$$4MnO_4^- + 12H^+ \leftrightarrow 4Mn^{2+} + 6H_2O + 5O_2 \ldots \text{Eq. (3)}$$

While the equilibrium concentration of Mn^{2+} is small, its production is considered to be rapid[55]. Therefore, the reaction between Mn^{2+} and MnO_4^- is the rate limiting step. This reaction is initially exceedingly slow, but is known to be autocatalytic, with MnO_2(s) surfaces substantially increasing the reaction rate[54,57,58]. The maximum rate of this reaction has been measured to scale as[54]

$$v_{max} = k_1 [MnO_4^-] ([Mn^{2+}] - k_2) ([MnO_2] + k_3) (1 + k_4[H^+])^{-1} \ldots \text{Eq. (4)}$$

The inverse of this rate is proportional to the induction time to initial MnO_2(s) formation. In our experiment, Mn^{2+} is produced by equilibrium in Eq. (3) rather than being deliberately added to the solution. Assuming that equilibrium (3) is established rapidly, $[Mn^{2+}] \sim [MnO_4^-][H^+]^3[O_2]^{-5/4}$ and the induction time scales approximately as

$$1/t_{induction} \sim [MnO_4^-]^2 [H^+]^2 ([MnO_2] + k) [O_2]^{-5/4} \ldots \text{Eq. (5)}$$

The strong dependence of the induction time on $[H^+]$ is qualitatively consistent with the dramatic sensitivity to *p*H we observe experimentally. However, the autocatalytic nature of this reaction implies that the concentration of $[MnO_4^-]$ vs. time should be sigmoidal[57,58], which is not consistent with the linear decrease in $[MnO_4^-]$ that we observe.

One possible reason for this apparent inconsistency in the evolution of $[MnO_4^-]$ with time is that in the *in situ* experiment, MnO_4^- may decompose photochemically by the known pathway:

$$MnO_4^- + h\nu \rightarrow MnO_2^- + O_2 \ldots \text{Eq. (6)}$$

where MnO_2^- persists in the solution for some time until finally precipitating as MnO_2(s)[59,60]. In acidic conditions, the reaction in Eq. (6) has been reported to be zero-order[59], analogous to our observations shown in Figure 5. However, the final reaction outcome is unchanged whether the reaction pathway is photochemically-active or thermally driven: in parallel *ex-situ* hydrothermal reactions where stainless-steel autoclaves are used, the same δ'-MnO_2 product was formed at *p*H 1.1[33] and no visually observable precipitation was found at *p*H 2.6. This agreement between the non-equilibrium reaction products obtained *in-situ* and *ex-situ* indicates that even if the initial decomposition of the MnO_4^- precursor is photochemically induced during the WAXS measurements, the formation of the solid product proceeds by the same mechanism in both cases.

Finally, it is possible that the linear decrease in $[MnO_4^-]$ arises from a convolution of multiple intermediates and thus does not represent a true zero-th order elementary reaction step. As discussed in Figure 7, the

nucleation of MnO_2 may be a multi-step reaction. Some Mn_{tet} may exist simultaneously in the solution, pre-nucleation clusters, and other reaction intermediates. The Mn_{tet} fraction obtained from the XAS data in Figure 5 is the summation of all Mn_{tet} in the abovementioned configurations, and could not be decoupled from the current data. Therefore, the linear decrease in Mn_{tet} concentration may arise from a convolution of multiple reaction steps instead of signifying a truly zero-order elementary reaction step. Future work should aim to ascertain insights on the chemical conversion kinetics of these transition metal complexes, as they play an important role in governing the induction times and transformation rates of metal oxide precipitation in an aqueous system.

■ Conclusions

The key conceptual breakthrough needed to achieve a theory of predictive synthesis is an ability to deconvolute the competing factors between the thermodynamics and kinetics of phase transformations. In this work, we investigated how experimentally observed precipitation conditions deviate from expectations for a thermodynamic Pourbaix diagram. Specifically, we investigated the induction of δ'-MnO_2 during hydrothermal synthesis at *p*H = 0.5–2.6. *In situ* WAXS and XAS were performed to monitor the crystallization process from MnO_4^- to δ'-MnO_2, in terms of onset time and the atomic fraction of tetrahedrally (or octahedrally) coordinated Mn. We observed two distinct kinetic regimes above and below *p*H 2, where the conversion kinetics of tetrahedrally-coordinated MnO_4^- to octahedrally-coordinated δ'-MnO_2 are distinctive. At lower *p*H, the reduction reaction is faster, which produces more Mn_{tet}-Mn_{oct} assemblies for the nucleation of the crystalline phase. This *p*H region corresponds to the boundary of a Metastable Zone Width in the Pourbaix diagram, which we measured to be near *p*H 2 in this experiment. Our kinetic analysis provides an important feature to consider when comparing experimental synthesis results with the calculated thermodynamic phase diagram, especially when anticipating the relative timeline for harvesting metastable or intermediate phases.

■ Author Contributions:

B.R.C., W.S., L.S., G.C., M.T., K.S., and D.K., originated the research. B.R.C. and L.S. performed in situ X-ray measurements and data analysis. K.S. designed the hydrothermal reactor. K.S. and R.D. supported the synchrotron-based WAXS and XAS experiments. W.S. and B.R.C. interpreted the thermodynamics and kinetics of the *in situ* observations. R. D. provided beamline support at the Stanford Synchrotron Radiation Lightsource. The manuscript was written by B.R.C., W.S., M.T., D.K., and L.S. All authors contributed to discussions of data and manuscript review.

Notes: The authors declare no competing financial interest.

■ Acknowledgements

This work was supported by Center for Next Generation Materials by Design: Incorporating Metastability, an Energy Frontier Research Center funded by the U.S. Department of Energy, Office of Science, Basic Energy Sciences under Award No. DEAC36-08GO28308. Use of the Stanford Synchrotron Radiation Lightsource, SLAC National Accelerator Laboratory, was supported by the U.S. Department of Energy, Office of Basic Energy Sciences under Contract No. DE-AC02-76SF00515. The authors would like to

thank Charles Troxel Jr. and Ross Arthur for helping build the hydrothermal reactor, as well Tim Dunn for beamline support.

■ Author Information

Corresponding Authors:

Bor-Rong Chen (Email: borrong.chen@inl.gov)

Wenhao Sun (Email: whsun@umich.edu)

Michael F. Toney (Email: michael.toney@colorado.edu)

Present Addresses:

Bor-Rong Chen is currently at *Energy Storage and Transportation Department, Energy and Environmental Science and Technology, Idaho National Laboratory, Idaho Falls, ID 83415, USA.*

Wenhao Sun is currently at *Department of Materials Science and Engineering, University of Michigan, Ann Arbor, Michigan, 48109, USA.*

Laura T. Schelhas is currently at *National Renewable Energy Laboratory, Golden, CO 80401, USA.*

Michael F. Toney is currently at *Department of Chemical and Biological Engineering, University of Colorado Boulder, Boulder, CO 80309, USA.*

■ Associated Content

Supporting Information accompanies this paper. Detailed experimental procedures and data analysis can be found in the Supporting Information document. This material is available free of charge via the Internet at http://pubs.acs.org.

■ References

1. Feng, S. H. & Li, G. H. *Hydrothermal and Solvothermal Syntheses*. *Modern Inorganic Synthetic Chemistry: Second Edition* (2017). doi:10.1016/B978-0-444-63591-4.00004-5.

2. Shi, W., Song, S. & Zhang, H. Hydrothermal synthetic strategies of inorganic semiconducting nanostructures. *Chem. Soc. Rev.* **42**, 5714–5743 (2013).

3. Feng, S. & Xu, R. New Materials in Hydrothermal Synthesis. *Acc. Chem. Res.* **34**, 239–247 (2001).

4. Whittingham, M. S. Hydrothermal synthesis of transition metal oxides under mild conditions. *Curr. Opin. Solid State Mater. Sci.* **1**, 227–232 (1996).

5. Sheets, W. C., Mugnier, E., Barnabé, A., Marks, T. J. & Poeppelmeier, K. R. Hydrothermal synthesis of delafossite-type oxides. *Chem. Mater.* **18**, 7–20 (2006).

6. Adschiri, T., Hakuta, Y. & Arai, K. Hydrothermal Synthesis of Metal Oxide Fine Particles at Supercritical Conditions. *Ind. Eng. Chem. Res.* **39**, 4901–4907 (2000).

7. Cundy, C. S. & Cox, P. A. The Hydrothermal Synthesis of Zeolites: History and Development from the Earliest Days to the Present Time. *Chem. Rev.* **103**, 663–702 (2003).

8. Lee, Y.-R., Kim, J. & Ahn, W.-S. Synthesis of metal-organic frameworks: A mini review. *Korean J. Chem. Eng.* **30**, 1667–1680 (2013).

9. Stein, A., Keller, S. W. & Mallouk, T. E. Turning Down the Heat : Design and Mechanism in Solid-State Synthesis. *Science (80-.).* **259**, 1558–1564 (1993).

10. Gopalakrishnan, J. Chimie Douce Approaches to the Synthesis of Metastable Oxide Materials. *Chem. Mater.* **7**, 1265–1275 (1995).

11. Zeng, Z. *et al.* Towards First Principles-Based Prediction of Highly Accurate Electrochemical Pourbaix Diagrams. *J. Phys. Chem. C* **119**, 18177–18187 (2015).

12. Huang, L. F. & Rondinelli, J. M. Electrochemical phase diagrams of Ni from ab initio simulations: Role of exchange interactions on accuracy. *J. Phys. Condens. Matter* **29**, (2017).

13. Huang, L. F. & Rondinelli, J. M. Electrochemical phase diagrams for Ti oxides from density functional calculations. *Phys. Rev. B - Condens. Matter Mater. Phys.* **92**, 1–13 (2015).

14. Persson, K. A., Waldwick, B., Lazic, P. & Ceder, G. Prediction of solid-aqueous equilibria: Scheme to combine first-principles calculations of solids with experimental aqueous states. *Phys. Rev. B - Condens. Matter Mater. Phys.* **85**, 235438 1–12 (2012).

15. Shoemaker, D. P. *et al.* In situ studies of a platform for metastable inorganic crystal growth and materials discovery. *Proc. Natl. Acad. Sci.* **111**, 10922–10927 (2014).

16. Haynes, A. S., Stoumpos, C. C., Chen, H., Chica, D. & Kanatzidis, M. G. Panoramic Synthesis as an Effective Materials Discovery Tool: The System Cs/Sn/P/Se as a Test Case. *J. Am. Chem. Soc.* **139**, 10814–10821 (2017).

17. Wang, X. & Li, Y. Synthesis and formation mechanism of manganese dioxide nanowires/nanorods. *Chem. - A Eur. J.* **9**, 300–306 (2003).

18. Xu, G. *et al.* Hydrothermal synthesis and formation mechanism of the single-crystalline Bi4Ti3O12nanosheets with dominant (010) facets. *CrystEngComm* **18**, 2268–2274 (2016).

19. Tang, Y. *et al.* Hydrothermal synthesis, evolution, and electrochemical performance of LiMn 0.5 Fe 0.5 PO 4 nanostructures . *Phys. Chem. Chem. Phys.* **17**, 18629–18637 (2015).

20. Sinha, A. K. *et al.* Thermodynamic and kinetics aspects of spherical MnO2 nanoparticle synthesis in isoamyl alcohol: An ex situ study of particles to one-dimensional shape transformation. *J. Phys. Chem. C* **114**, 21173–21183 (2010).

21. Testino, A., Buscaglia, V., Buscaglia, M. T., Viviani, M. & Nanni, P. Kinetic modeling of aqueous and hydrothermal synthesis of barium titanate (BaTiO3). *Chem. Mater.* **17**, 5346–5356 (2005).

22. Denkewicz, R. P., TenHuisen, K. S. & Adair, J. H. Hydrothermal Crystallization Kinetics of m-ZrO2and t-ZrO2. *J. Mater. Res.* **5**, 2698–2705 (1990).

23. Jensen, K. M. Ø., Tyrsted, C., Bremholm, M. & Iversen, B. B. In Situ studies of solvothermal synthesis of energy materials. *ChemSusChem* **7**, 1594–1611 (2014).

24. Becker, J. *et al.* Experimental setup for in situ X-ray SAXS/WAXS/PDF studies of the formation and growth of nanoparticles in near-and supercritical fluids. *J. Appl. Crystallogr.* **43**, 729–736 (2010).

25. Jensen, K. M. Ø. *et al.* Mechanisms for Iron Oxide Formation under Hydrothermal Conditions: An in Situ Total Scattering Study. *ACS Nano* **8**, 10704–10714 (2014).

26. Bøjesen, E. D. & Iversen, B. B. The chemistry of nucleation. *CrystEngComm* vol. 18 8332–8353 (2016).

27. Juhas, P. *et al.* Revealing the Mechanisms behind SnO2 Nanoparticle Formation and Growth during Hydrothermal Synthesis: An In Situ Total Scattering Study. *J. Am. Chem. Soc.* **134**, 6785–6792 (2012).

28. Zhu, M. *et al.* Precipitation pathways for ferrihydrite formation in acidic solutions. *Geochim. Cosmochim. Acta* **172**, 247–264 (2016).

29. Nývlt, J., Rychlý, R., Gottfried, J. & Wurzelová, J. Metastable zone-width of some aqueous solutions. *J. Cryst. Growth* **6**, 151–162 (1970).

30. Mersmann, A. & Bartosch, K. How to predict the metastable zone width. *J. Cryst. Growth* **183**, 240–250 (1998).

31. Ramakers, L. A. I. *et al.* Investigation of Metastable Zones and Induction Times in Glycine Crystallisation across Three Different Antisolvents. *Cryst. Growth Des.* (2020) doi:10.1021/acs.cgd.9b01493.

32. Sun, W., Kitchaev, D. A., Kramer, D. & Ceder, G. Non-equilibrium crystallization pathways of manganese oxides in aqueous solution. *Nat. Commun.* **10**, 573 (2019).

33. Chen, B. R. *et al.* Understanding crystallization pathways leading to manganese oxide polymorph formation. *Nat. Commun.* **9**, (2018).

34. Polte, J. Fundamental growth principles of colloidal metal nanoparticles - a new perspective. *CrystEngComm* **17**, 6809–6830 (2015).

35. Chu, D. B. K., Owen, J. S. & Peters, B. Nucleation and Growth Kinetics from LaMer Burst Data. *J. Phys. Chem. A* **121**, 7511–7517 (2017).

36. Sun, W. & Ceder, G. Induction time of a polymorphic transformation. *CrystEngComm* **19**, 4576–4585 (2017).

37. Toby, B. H. & Von Dreele, R. B. GSAS-II : the genesis of a modern open-source all purpose crystallography software package. *J. Appl. Crystallogr.* **46**, 544–549 (2013).

38. Ravel, B. & Newville, M. ATHENA , ARTEMIS , HEPHAESTUS : data analysis for X-ray absorption spectroscopy using IFEFFIT. *J. Synchrotron Radiat.* **12**, 537–541 (2005).

39. Yamamoto, T. Assignment of pre-edge peaks in K-edge x-ray absorption spectra of 3d transition metal compounds: electric dipole or quadrupole? *X-Ray Spectrom.* **37**, 572–584 (2008).

40. Chalmin, E., Farges, F. & Brown, G. E. A pre-edge analysis of Mn K-edge XANES spectra to help determine the speciation of manganese in minerals and glasses. *Contrib. to Mineral. Petrol.* **157**, 111–126 (2009).

41. Hanson, H. & Beeman, W. W. The Mn K absorption edge in manganese metal and manganese compounds. *Phys. Rev.* **76**, 118–121 (1949).

42. State, S. & Related, P. High-accuracy bond lengths from EXAFS of solid KMnO 4 and MnO 4- in aqueous solution. (1979).

43. Farges, F. Ab initio and experimental pre-edge investigations of the Mn K -edge XANES in oxide-type materials. 1–14 (2005) doi:10.1103/PhysRevB.71.155109.

44. D'Angelo, P., Roscioni, O. M., Chillemi, G., Longa, S. Della & Benfatto, M. Detection of second hydration shells in ionic solutions by XANES: Computed spectra for Ni2+ in water based on molecular dynamics. *J. Am. Chem. Soc.* **128**, 1853–1858 (2006).

45. Fulton, J. L., Heald, S. M., Badyal, Y. S. & Simonson, J. M. Understanding the effects of concentration on the solvation structure of Ca2+ in aqueous solution. I: The perspective on local structure from EXAFS and XANES. *J. Phys. Chem. A* **107**, 4688–4696 (2003).

46. Danilidis, I., Davenport, A. J. & Sykes, J. M. Characterisation by X-ray absorption near-edge spectroscopy of KMnO4-based no-rinse conversion coatings on Al and Al alloys. *Corros. Sci.* **49**, 1981–1991 (2007).

47. Liang, X. *et al.* Coupled morphological and structural evolution of δ-MnO2 to α-MnO2 through multistage oriented assembly processes: The role of Mn(iii). *Environ. Sci. Nano* **7**, 238–249 (2020).

48. Yin, B., Zhang, S., Jiang, H., Qu, F. & Wu, X. Phase-controlled synthesis of polymorphic MnO 2 structures for electrochemical energy storage. *J. Mater. Chem. A* **3**, 5722–5729 (2015).

49. De Yoreo, J. J. *et al.* Crystallization by particle attachment in synthetic, biogenic, and geologic environments. *Science (80-.).* **349**, (2015).

50. Smeets, P. J. M. *et al.* A classical view on nonclassical nucleation. *Proc. Natl. Acad. Sci. U. S. A.* **114**, E7882–E7890 (2017).

51. Gebauer, D., Völkel, A. & Cölfen, H. Stable prenucleation calcium carbonate clusters. *Science (80-.).* **322**, 1819–1822 (2008).

52. Peng, Y. *et al.* Two-step nucleation mechanism in solid-solid phase transitions. *Nat. Mater.* **14**, 101–108 (2015).

53. Henzler, K. *et al.* Supersaturated calcium carbonate solutions are classical. *Sci. Adv.* **4**, 1–12 (2018).

54. Tompkins, F. C. The kinetics of the reaction between manganous and permanganate ions. *Trans. Faraday Soc.* **38**, 131–139 (1941).

55. Ladbury, J. W. & Cullis, C. F. Kinetics and Mechanism of Oxidation by Permanganate. *Chem. Rev.* **58**, 403–438 (1958).

56. Adamson, A. W. The kinetics of the manganous-permanganate reaction. *J. Phys. Colloid Chem.* **55**, 293–303 (1951).

57. Zhao, L. Z., Young, V. Y. & Davis, J. G. Effect of Dispersed Manganese Oxides on the Decomposition of Permanganate Solutions. *Langmuir* **6**, 168–172 (1990).

58. Polissar, M. J. The kinetics of the reaction between permanganate and manganous ions. *J. Phys. Chem.* **39**, 1057–1066 (1935).

59. Lee, D. G., Moylan, C. R., Hayashi, T. & Brauman, J. I. Photochemistry of Aqueous Permanganate Ion. *J. Am. Chem. Soc.* **109**, 3003–3010 (1987).

60. Zimmerman, G. Photochemical decomposition of aqueous permanganate ion. *J. Chem. Phys.* **23**, 825–832 (1955).